A 10 mK scanning tunneling microscope operating in ultra high vacuum and high magnetic fields

Maximilian Assig, Markus Etzkorn, Axel Enders' , Wolfgang Stiepany, Christian R. Ast' , and Klaus Kern

Citation: Review of Scientific Instruments **84**, 033903 (2013); doi: 10.1063/1.4793793
View online: http://dx.doi.org/10.1063/1.4793793
View Table of Contents: http://aip.scitation.org/toc/rsi/84/3
Published by the American Institute of Physics

A 10 mK scanning tunneling microscope operating in ultra high vacuum and high magnetic fields

Maximilian Assig,[1] Markus Etzkorn,[1] Axel Enders,[1,a)] Wolfgang Stiepany,[1] Christian R. Ast,[1,b)] and Klaus Kern[1,2]
[1]*Max-Planck-Institut für Festkörperforschung, 70569 Stuttgart, Germany*
[2]*Institut de Physique de la Matière Condensée, Ecole Polytechnique Fédérale de Lausanne, 1015 Lausanne, Switzerland*

(Received 20 December 2012; accepted 16 February 2013; published online 8 March 2013)

We present design and performance of a scanning tunneling microscope (STM) that operates at temperatures down to 10 mK providing ultimate energy resolution on the atomic scale. The STM is attached to a dilution refrigerator with direct access to an ultra high vacuum chamber allowing *in situ* sample preparation. High magnetic fields of up to 14 T perpendicular and up to 0.5 T parallel to the sample surface can be applied. Temperature sensors mounted directly at the tip and sample position verified the base temperature within a small error margin. Using a superconducting Al tip and a metallic Cu(111) sample, we determined an effective temperature of 38 ± 1 mK from the thermal broadening observed in the tunneling spectra. This results in an upper limit for the energy resolution of $\Delta E = 3.5 k_B T = 11.4 \pm 0.3\,\mu$eV. The stability between tip and sample is 4 pm at a temperature of 15 mK as demonstrated by topography measurements on a Cu(111) surface. © *2013 American Institute of Physics*. [http://dx.doi.org/10.1063/1.4793793]

I. INTRODUCTION

Since its invention, scanning tunneling microscopy (STM) has evolved into one of the most versatile surface science analysis tools.[1–6] It offers a high degree of lateral control with simultaneous spectroscopic capabilities at the atomic scale.[7–9] For metallic tips the energy resolution of spectroscopic measurements is limited by the thermal broadening of the Fermi edge given by $\Delta E = 3.5 k_B T$, where T is the temperature of the tunneling electrons.[10] For the lowest lying energy scales such as the level splitting due to the hyperfine interaction or the Zeeman splitting in a magnetic field, an extremely high energy resolution is necessary demanding the lowest temperatures. For example, the hyperfine splitting of bismuth atoms in silicon has been calculated to be 30 μeV,[11] which requires temperatures well below 100 mK for this to be observed in inelastic tunneling spectroscopy. The Zeemann splitting (Bohr magneton: $\mu_B = 57.9\,\mu$eV/T) of the superconducting quasiparticle density of states (DOS) is well studied in planar tunnel junctions.[12–14] It could serve as a local probe for the spin-polarization of the tunneling electrons using a superconducting STM tip. So far, only few STM setups have been realized for temperatures at or below 100 mK.[15–17] Very few systems have a direct connection to an ultra high vacuum (UHV) chamber because of the complexity of such a setup.[18,19] In this article, we describe the design of a mK-STM with direct access from a UHV chamber into the cryostat optimized for ultra-high vacuum sample preparation, high magnetic fields, and fast turn over times for tip and sample exchange.[20] The dilution cryostat will be discussed emphasizing design features including the temperature measurement and wiring concept. Finally, we report on the performance of the mK-STM.

II. THE SCANNING TUNNELING MICROSCOPE

A three-dimensional model of the STM unit is shown in Fig. 1(a). It consists of the STM base plate, the scan assembly, a conical housing (with a cross sectional view to reveal the inside), the sample section at the bottom, and the transfer guiding cone. The STM has been constructed from oxygen-free, high conductivity copper (OFHC) and coin silver, which is a 93.5% Ag and 6.5% Cu alloy. The copper parts are gold plated, without using a Ni wetting layer in between. Aluminum nitride (Shapal M) or crystalline aluminum oxide (sapphire) have been used as insulating materials. The transfer guiding cone, aligning the axes of the transfer tool and the STM unit, is made of Ti reducing its total weight. For gluing UHV compatible components, electrically insulating epoxy has been used.

The STM unit is assembled on the base plate shown in Fig. 1(b). All electrical connections are interfaced at this plate with home built single wire and coaxial connectors allowing fast and easy exchange of scan heads. For this reason guiding pins are mounted on top of the base plate so that the complete STM head can be exchanged blindly without disassembling the cryostat. The scan assembly and the conical housing (not shown in Fig. 1(b)) are attached to the base plate. The conical housing has been optimized in design so that the response of the tip-sample distance to external vibrations is minimized.[21]

In Fig. 1(c) the interface plate is shown, to which the STM base plate is connected. Four rods, along which the wiring is guided to the interface plate, extend rigidly from the center of the magnetic field, where the STM is located, to the mixing chamber, which is the cold spot of the cryostat

a)Present address: Department of Physics and Astronomy, University of Nebraska, Lincoln, Nebraska 68588, USA.
b)Author to whom correspondence should be addressed. Electronic mail: c.ast@fkf.mpg.de.

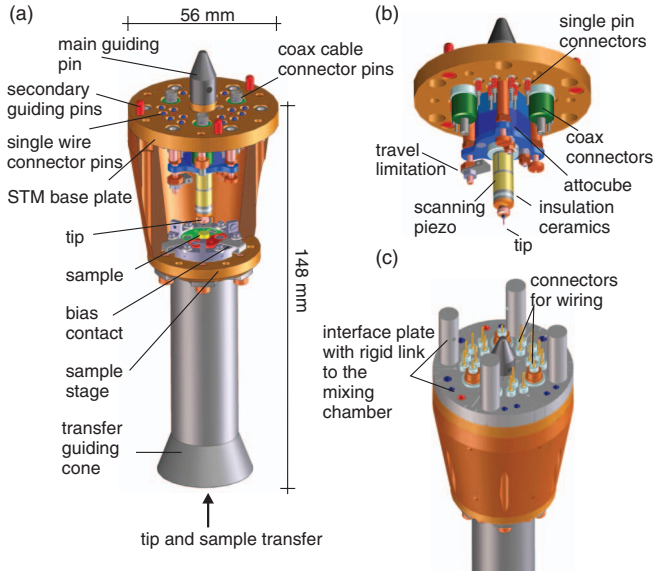

FIG. 1. STM scan head. (a) Overview of the STM scan head. The outer housing is cut open in the image. (b) View to the interior of the STM unit. (c) Perspective view of the STM unit connected to the four posts of the link structure to the mixing chamber.

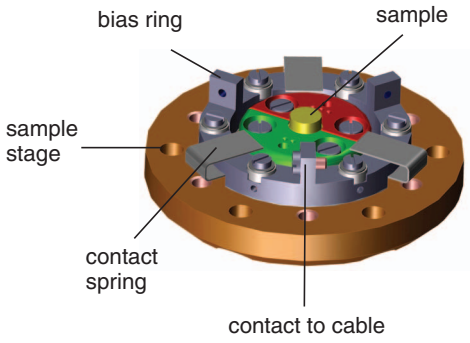

FIG. 3. The sample section which is mounted to the outer housing of the STM scan head contains an inner thread for the sample holder. An electrically insulating contact ring is mounted to the sample stage with three springs to contact the sample.

(see also Fig. 6). No internal damping mechanism, such as springs, has been implemented to maximize the thermal contact between mixing chamber and STM.

The scan assembly holding tip and scan piezo is mounted on a coarse motor,[22] which is fixed to the inside of the STM base plate (see also Fig. 1(b)). Three posts act as travel limitation during coarse approach and tip transfer. A cross sectional view of tip and scan piezo is shown in Fig. 2(a). The scan piezo is a tube for scanning in x-, y-, and z-direction. It is mounted on a base plate via a ceramic insulator. A receptacle for the tip holder is attached to the top of the piezo tube by a second ceramics. The tip holder (Fig. 2(b)) has a spring loaded shaft, which is inserted into the receptacle like a banana plug. It has an outer thread which is used for the transfer tool to attach. A thin capillary holding the tip is attached to the tip holder.

Figure 3 shows a close up of the sample section mounted below the conical housing of the STM unit. The sample section is a metal plate with an inner thread for the sample holder. A bias ring, to which the bias voltage cable is attached surrounds the threaded hole. Three flat contact springs are used to ensure that both thermoelement half discs (see below) are contacted avoiding thermovoltages across the sample holder. The bias ring is insulated from the sample section plate only by a thin Kapton foil in order to maximize thermal conductivity.

We have designed two different sample holders, one optimized for electron beam heating of metal samples and one for direct current heating of semiconducting samples (Fig. 4). Both designs have identical base bodies with a hexagonal opening accepting the transfer tool and an outer thread fitting into the sample stage. An insulating sapphire plate is placed on top of the base body. The sample is mounted on top of this plate (Fig. 4(c)). It is held in position by two half discs, which are in electrical contact with the sample, but insulated from the base body. For metallic samples, the half discs are made of thermoelement material in order to be able to measure the temperature of the sample during heating (Figs. 4(b) and 4(c)). We use a Type S (Pt-Pt90Rh10) thermocouple suitable for temperatures up to 1600 °C, and compatible with temperatures down to the low mK range (no magnetic ordering). To increase the efficiency of the electron heating, we have installed a molybdenum electron collector at the back of the sample reducing the electron traveling length. In the design for direct current heating, the half discs contacting the sample are made of molybdenum (Figs. 4(d) and 4(e)). The sample is pushed against the half discs from below by the

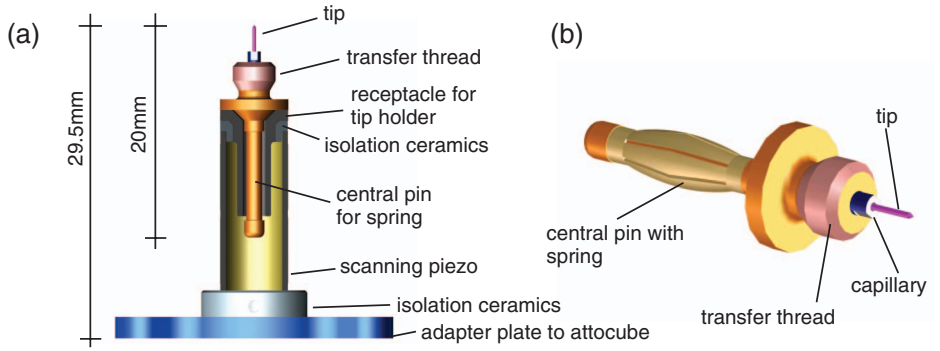

FIG. 2. Scan assembly. (a) Scanning piezo is attached to the adapter plate via an insulation ceramic. It carries the receptacle for the tip holder. The whole scan assembly is mounted to an attocube coarse motor (not shown). (b) Close up of the tip holder.

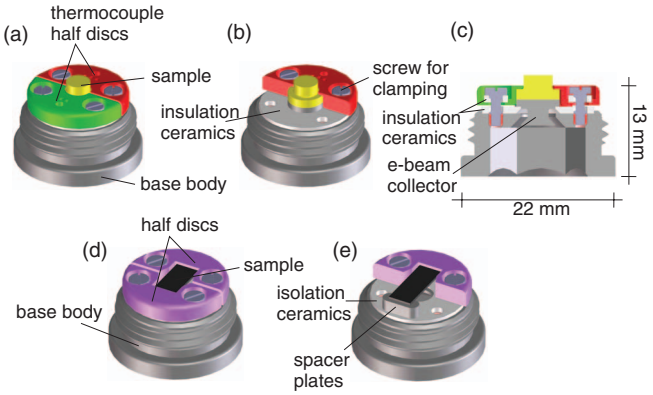

FIG. 4. Sample holder. (a) Completely assembled sample holder for e-beam heating. The base of the sample holder is a body containing an outer thread fitting into the sample section. An e-beam collector and the sample are clamped to the base body by two half discs made of thermoelement material. (b) One half disc is removed. A sapphire plate is used to insulate the sample and e-beam collector from the base body. (c) Cross section through the sample holder. (d) Perspective view of the sample holder adapted for semiconducting samples. The half discs fixing the sample to the base body are made of molybdenum. (e) Spacer platelets compensate for different wafer thickness.

spring force of small spacer platelets in order to allow for the sample to thermally expand reducing the risk of deformation.

Tips and samples are transferred through the bottom of the cryostat. This greatly reduces the transfer length as opposed to a top loading design. Due to the geometry of the cryostat there is no visual access to the scan head during the transfer procedure. To ensure a safe transfer, two PEEK alignment rings center the axis of the transfer tool into the transfer cone of the STM unit. Solid state joints below the alignment rings (not shown) capable of transferring torque, but otherwise flexible can compensate a small misalignment. The head of the transfer tool has the shape of an Allen key, fitting into the back of the sample (see Fig. 5(b)). The head has a threaded hole to accept the tip holder (see Fig. 5(c)). The tip apex is inside this threaded hole, so that it is optimally protected during the transfer procedure.

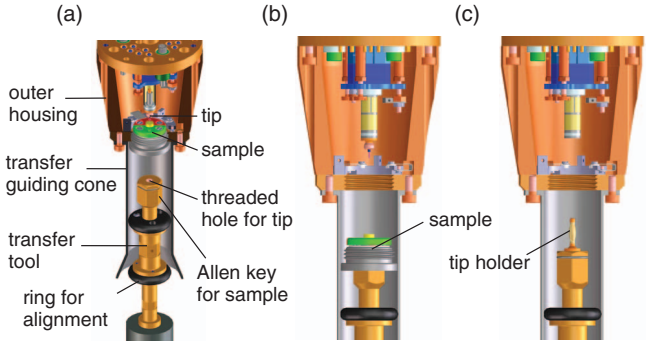

FIG. 5. Tip and sample transfer. (a) The transfer tool is moved into the STM unit through the guiding cone. The transfer head is an Allen key fitting into the back of the sample holder. A threaded hole on top is used for accepting the tip holder. Two alignment rings slide into the transfer guiding cone ensuring alignment of the axes. (b) The sample is transferred to the STM. (c) The tip is removed from the STM.

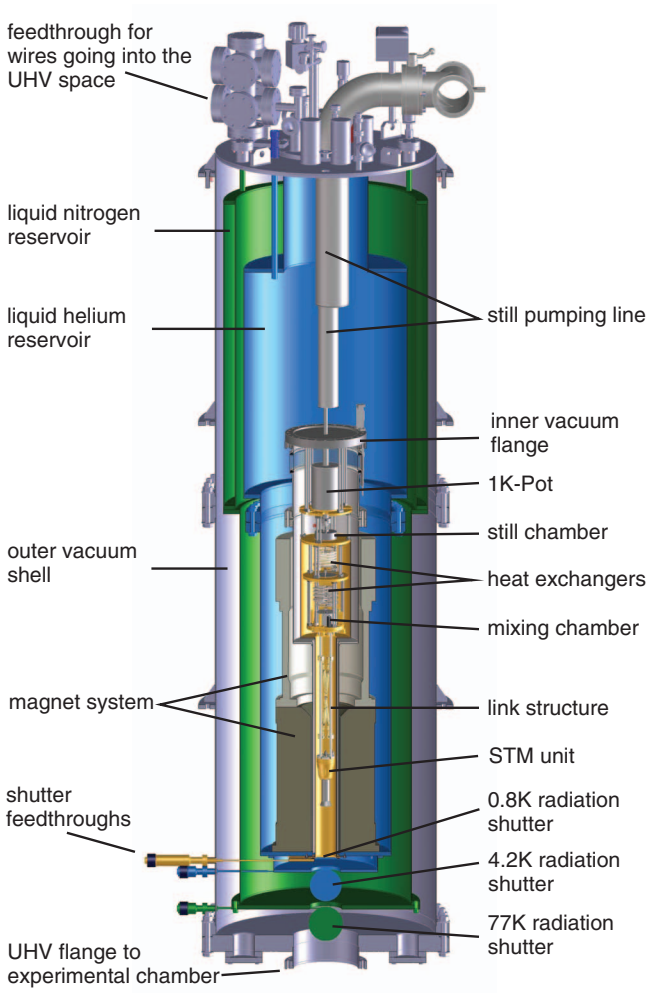

FIG. 6. Cross sectional view through the complete cryostat.

III. THE DILUTION REFRIGERATOR

Generating temperatures continuously below 100 mK with high cooling power requires dilution refrigeration.[23,24] The refrigerant is a ^{3}He/^{4}He mixture which starts to separate into two phases at temperatures below 800 mK: a concentrated (^{3}He rich) and a diluted (^{4}He rich) phase. The cooling process relies on the different enthalpy for ^{3}He atoms within the two phases. The phase separation as well as the cooling takes place in the mixing chamber (MC), which is the coldest spot in the dilution refrigerator. A technical realization of dilution refrigeration was first reported by Das *et al.* in 1965.[25] Reviews on the theoretical and technical aspects can be found in Refs. 26–30.

A cut through our dilution refrigerator, which is a custom designed model fabricated by Janis Research Company,[31] is shown in Fig. 6. The cryostat is UHV compatible with liquid nitrogen (LN_2) and liquid helium (LHe) reservoirs acting as thermal radiation shields. The whole cryostat can be baked to 100 °C limited by the materials used in the magnet design. A solenoid magnet, a saddle coil, as well as a compensation coil are welded into the LHe reservoir. Magnetic fields up to 14 T (0.5 T) can be generated perpendicular (in one direction parallel) to the sample surface. At the same time we can compensate the large stray fields of the solenoid magnet in the

region of the MC. The dilution unit is mounted to the UHV side of the inner vacuum flange above the magnet (see Fig. 6). All pipes for the operation of the dilution cycle as well as cables for cryostat and STM operation are fed through the inner vacuum flange (not shown).

The dilution unit consists of a 1K pre-cooling stage in combination with the condenser impedance ($Z = 3 \times 10^{10}\,\mathrm{cm}^{-3}$), a still chamber, where the fluid level of the diluted phase is located, and a heat exchanger section with the mixing chamber, below which the link structure and the STM are mounted (Fig. 6). The 1K pre-cooling stage consists of a large volume 1K-pot with an acoustic noise reducer. The noise reducer is intended to condense any gas bubble, which may occur during liquid ^{4}He expansion, before the bubble could enter the 1K-pot volume (whistle effect). In this way, we are able to leave the 1K-pot running during measurements. To minimize heat input from thermal radiation, the MC and STM are protected by radiation shields anchored at the LN_2-reservoir (77 K), the LHe-reservoir (4 K), and the still chamber (800 mK). Access through the radiation shields for tip and sample transfer is given by shutter mechanisms. The UHV preparation chamber connects to the bottom flange of the cryostat.

Temperature measurements are performed using resistive and magnetic thermometry.[32] The resistive temperature sensors are based on ruthenium oxide (RuO) clusters in a glass matrix.[33–36] While the RuO sensors are the workhorse in routine cryostat operation down to 30 mK,[37] the lower temperatures of the mixing chamber require sensors less susceptible to saturation effects. Janis Research Company provides a solution with a pair of mutual inductance sensors.[38] The susceptibility of a paramagnetic cerium magnesium nitrate salt (CMN) follows the Curie-Weiss law with 5% accuracy down to about 5 mK.[27,39] The corresponding fitting function contains only two fitting parameters. These are obtained from the known superconducting transition temperatures (see Table I) in a Fixed Point Device (FPD), where different seeds of superconducting compounds are compressed into silver powder. In the FPD, the transitions are seen as jumps in the mutual inductance due to the Meissner effect. A typical calibration curve is shown in Fig. 7, where the black line is the Curie-Weiss law used to interpolate and extrapolate the scale for a continuous temperature reading from 1 K down to about 8 mK. The typical relaxation time of the CMN sensor is about 150 s near 10 mK.

Different RuO temperature sensors are positioned at various temperature levels of the dilution stage (at the 1K-pot level, still chamber, heat exchanger section, MC and STM

TABLE I. Some of the superconducting compounds and the corresponding superconducting transition temperatures in the FPD temperature sensor.

Superconducting impurity	Transition temperature (mK)
Cd	520
$AuIn_2$	208
$AuAl_2$	161
Ir	96

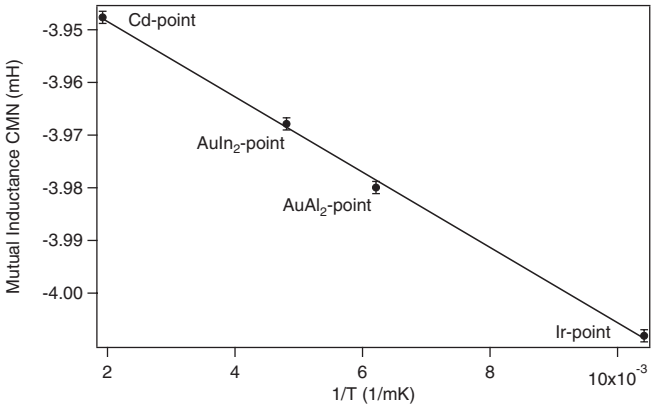

FIG. 7. Calibration curve of the CMN magnetization thermometer. Magnetization values are plotted against the inverse transition temperature of the superconducting compounds in the fixed point device (see text for details).

support). In the RuO sensor, the electron transport is due to thermally activated electrons, which hop between energy states localized at the RuO clusters near the Fermi level (Mott hopping). We calibrate the RuO temperature sensor at MC and STM support against the CMN temperature sensor.[40] In this way, we get a set of temperature (T) and resistance (R) values which are expected to follow the Mott hopping law[41]

$$\sigma = \frac{1}{R} = A_0 \exp\left[-\left(\frac{A_1}{T}\right)^{\gamma}\right], \tag{1}$$

where A_0 is a scaling factor, A_1 depends on the DOS near the Fermi level as well as the decay length of the wave functions of the localized states. The temperature exponent γ is expected to be 1/2 for pure Mott hopping. However, including Coulomb interaction results in $\gamma \approx 1/4$ (Efros-Shklovskii hopping).[42] At very low temperatures the resistance curves of the temperature sensors deviate from the standard Mott model. To account for these deviations we use a phenomenological extension to the above formula:

$$\sigma = \frac{1}{R} = A_0 \exp\left[-\left(\frac{A_1}{T - T_0}\right)^{\gamma}\right] + \sigma_0. \tag{2}$$

Here, σ_0 is a temperature independent conductivity, which is attributed to percolation paths within the glass matrix and temperature independent tunneling. The value T_0 is used to describe a faster saturation of the conductivity than suggested by the Mott hopping law. It is not to be regarded as an experimental offset to compensate for calibration errors. The saturation can be physically motivated by additional localization effects at low temperatures (e.g., Anderson localization). However, we also found that the parameters σ_0 and T_0 depend on the local environment, in which the sensor is located. In Fig. 8(a) the obtained resistance values are plotted against the MC temperature which is measured by the CMN temperature sensor. The black lines are the fit to the data using the inverse function of Eq. (2), i.e., T(R). The relative deviation between fit and measured temperature is shown in Fig. 8(b). The fit coefficients are summarized in Table II. It turns out that the modified Mott hopping law with the two additional parameters yields a much better agreement with the data in the temperature region below 35 mK.

TABLE II. Fitting coefficients for the temperature calibration of the resistive temperature sensors at MC and STM support.

Sensor	$A_0 \times 10^{-3}$ (Ω^{-1})	$A_1 \times 10^3$ (mK)	γ	$\sigma_0 \times 10^{-6}$ (Ω^{-1})	T_0 (mK)
MC	8.1 ± 0.1	64.7 ± 0.5	0.258 ± 0.001	1.04 ± 0.03	11.8 ± 0.4
STM support	6.0 ± 0.1	30.6 ± 0.5	0.283 ± 0.001	1.70 ± 0.03	9.6 ± 0.4

The cryostat performance is characterized by its base temperature and cooling power $\dot{Q}$. In a dilution cryostat the latter depends on the ^{3}He circulation $\dot{n}$.[19,26,27] Heating the still chamber increases $\dot{n}$, which increases $\dot{Q}$ resulting in a lower MC temperature[26,27] until the heat load from the ^{3}He input becomes too high and the MC temperature increases again. Optimum circulation is achieved when these two contributions are in balance. The MC temperature of our cryostat as a function of the ^{3}He circulation $\dot{n}$ shown in Fig. 9 indicates a clear minimum. Fitting with a second order polynomial, we find that the optimal circulation is $\dot{n} = 160 \pm 1\ \mu$mol/s at which we reach a base temperature of 11.4 ± 0.3 mK. The cooling power of our cryostat at 100 mK, which we determined by measuring the heater power needed to stabilize the MC at this temperature, is $396 \pm 5\ \mu$W.

IV. IMPLEMENTATION OF THE mK-STM

Concerning the wiring of cryostat and STM, eighteen unshielded wires in twisted pair configuration and three shielded cables (for bias voltage, tunneling current and z-signal of the scan tube) are connected to the STM unit. Care was taken not to interrupt the shielding of the coaxial cables at any point down to the STM to reduced the noise pick-up for the most sensitive signals. Low thermal conductivity materials have been used for cables and wires from room temperature to the MC to minimize the heat load. In our system, we use stainless steel coaxial cables and manganine (Cu86Mn12Ni2) twisted pair wires. The only exception to the wiring scheme mentioned above are the electrical connections to the coarse motor. In order to keep the rising edge of the signal for the slip-stick motion as steep as possible, the total resistance for the coarse motor wires should not exceed 10 Ω. Therefore, we use thin copper wires from room temperature to the 1 K pot stage and proceed with superconducting wires to block heat transport along these lines to the MC. All cables are thermally anchored at every stage down to the MC. From the MC to the STM high thermal conductivity is desired. For the unshielded wires we use Kapton insulated silver wires. For the shielded cables we use semi-rigid copper cables in the support structure and coaxial cables with copper inner conductor and a gold plated copper braid within the STM scan head.

To avoid ground loops, we have chosen the cryostat to be the common grounding point. We took care to electrically isolate it from the environment, so that the cryostat is completely electrically floating except for one low resistance connection to ground. To avoid high frequency pick-up, all lines entering the cryostat are electrically filtered at the room temperature feedthroughs by commercially available π-filters[43,44] in series with a resistor to achieve a cut-off frequency of 10 kHz. Within the cryostat, no internal cryogenic filters are used other than the intrinsic distributed RC-filters of the coaxial cables.

The UHV preparation chamber is mounted to the bottom flange of the cryostat. It allows standard UHV preparation like sputtering, sample annealing, deposition of materials, and UHV cleaving. A load-lock attached to the UHV chamber allows to transfer samples, tips and filament units (see below) from ambient conditions into UHV. Along with the two different designs of the sample holders mentioned above, we developed two sample preparation stages, one for electron

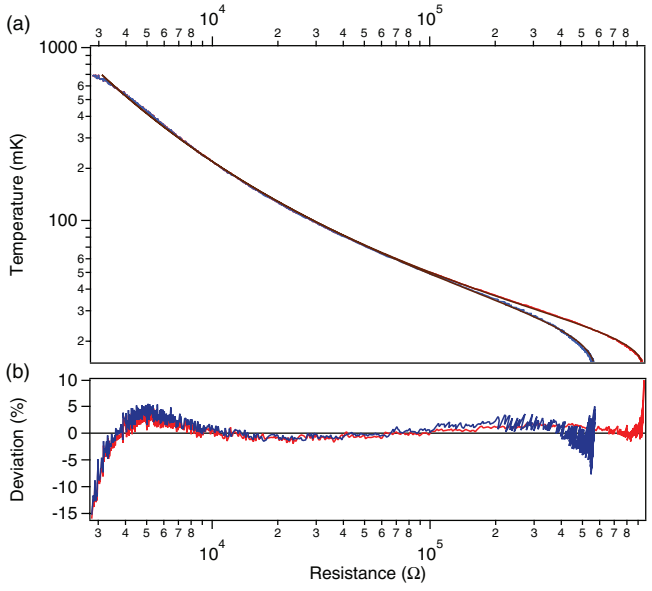

FIG. 8. Calibration curves of the RuO temperature sensors. (a) Temperature calibration curves. Red: data from RuO sensor at MC, blue: data for RuO sensor at the interface plate, black: fit to the data. (b) Relative deviations between fitting curves and measured data. The fits lie very well on the data below 500 mK with less than 5% of error.

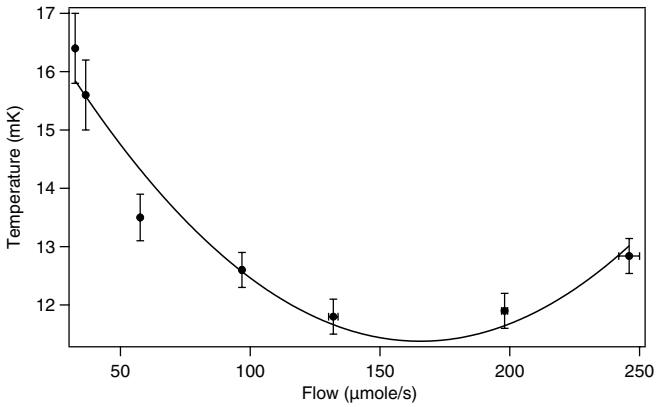

FIG. 9. MC temperature as a function of the ^{3}He circulation. There is a clear minimum for circulation rates between about 130 μmol/s and 200 μmol/s. The cryostat is normally operated at lowest circulation rate at a temperature of about 15 mK.

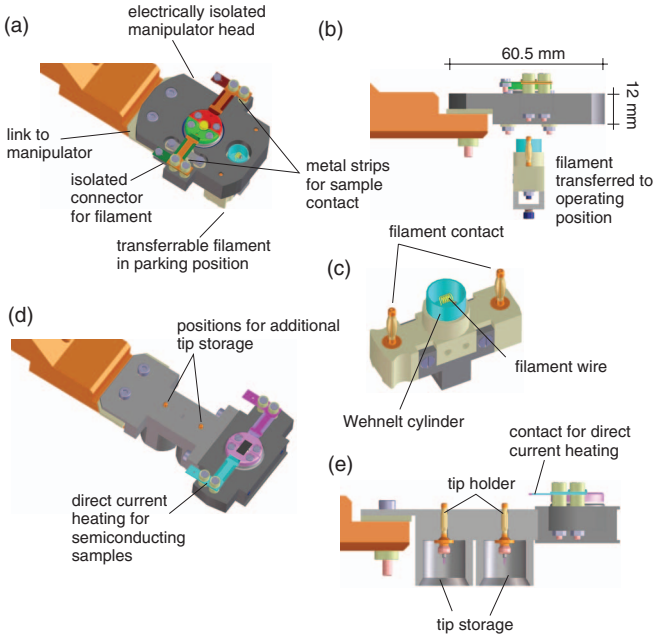

FIG. 10. Sample preparation stages for electron beam and direct current heating. (a) Perspective view and (b) side view of the preparation stage for electron beam heating. The stage is connected through an electric insulator to the manipulator. The sample is in the stage. For temperature measurements the thermoelement half discs of the sample holder are used. The filament for sample annealing is transferred to the operating position from below. (c) Perspective view of the filament with the two banana plug pins for the electrical contacts on the side, which also hold the filament in place. (d) Perspective view and (e) side view of the preparation stage for direct current heating. Two tip holders in parking positions are shown as well.

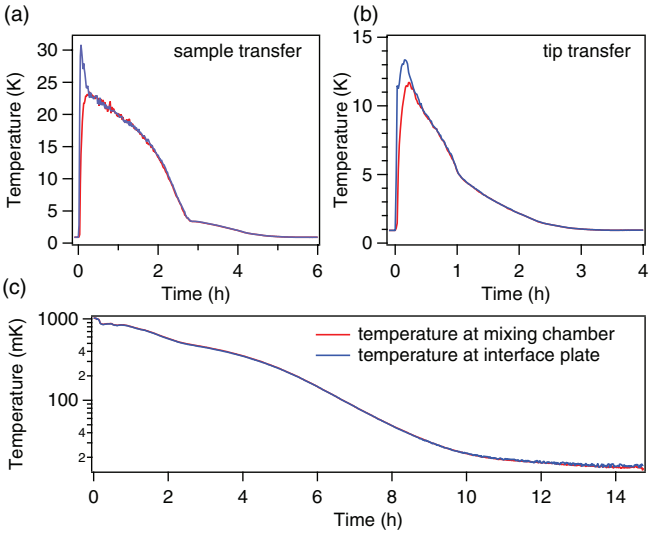

FIG. 11. Cool down times after tip and sample transfer. Red curve: temperature at the MC. Blue curve: temperature at interface plate. (a) Cool down after tip transfer to approximately 1 K with an initial tip temperature of 300 K. (b) Cool down after sample transfer with an initial sample temperature of 100 K. (c) Cool down from 1 K to base temperature using the dilution cycle.

beam heating (Fig. 10(a)) and one for direct current heating (Fig. 10(b)). In both, two small metal strips make electrical contact to the half discs on the sample holder when it is inserted. For the direct current heating, the strips are made out of molybdenum in order to pass high currents through the sample. For the electron beam heating stage the contact strips are made of type S thermoelement material, the same as for the sample holder. For sample heating, a filament holder is plugged into the preparation stage underneath the sample. In Fig. 10(c) the filament holder is shown with the transfer process displayed schematically in Fig. 10(d). For maintenance purposes it can be transferred into the load lock and repaired *ex situ*. A metal cylinder embedded into the filament holder which is the same electric potential as the filament wire (Wehnelt cylinder) focuses the electrons onto the sample. This significantly enhances the efficiency of the electron beam heating. In our design, filament and Wehnelt cylinder are on negative high voltage so that the sample and the thermoelements can be kept on ground potential.

Tips and samples are transferred from the preparation chamber into the STM by a magnetically coupled transfer manipulator. We typically do not precool the tips before transfer as their heat capacity is small enough to cool quickly. Samples are cooled to 100 K before transfer to reduce the thermalization time. The temperature of the MC and STM before the transfer is around 800 mK as we have to take out most of the mixture to ensure a safe transfer. In Fig. 11 the thermalization period after tip and sample transfer is shown. The system cools back to roughly 800 mK after a tip (sample) transfer within a period of 3 h (5 h) as indicated in Figs. 11(a) and 11(b). From 800 mK we cool to a temperature below 15 mK within roughly 10 h.

To achieve a low vibration level for STM measurements, we decoupled the whole system from the building (see also Fig. 12). Starting from the building level (brown), a set of active dampers isolate the first damping level (red) in a frequency range from 0.6 to 100 Hz. From here a passive

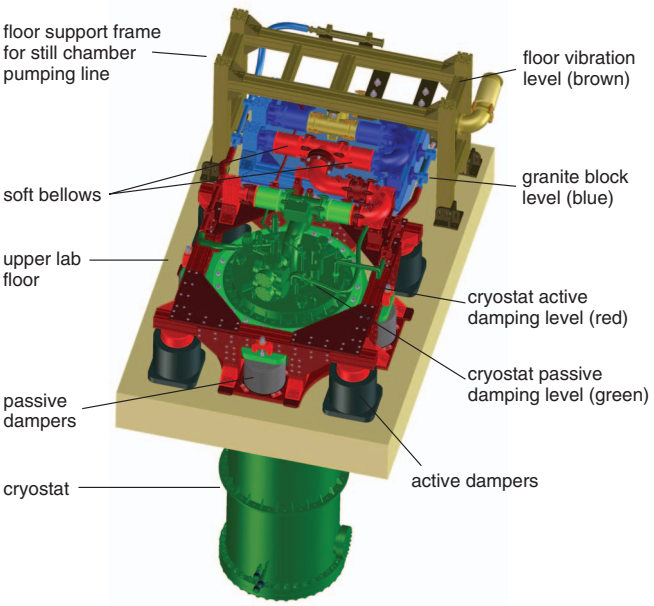

FIG. 12. Schematic of the different vibration levels. For damping the cryostat a combination of active controlled and passive dampers are used. The colors are chosen to illustrate the different levels of vibration isolation. Vibrations transmitted through the pumping lines are eliminated by attaching the lines to a massive granite block. For the still pumping line soft bellow segments are used to reduce the coupling among the various stages.

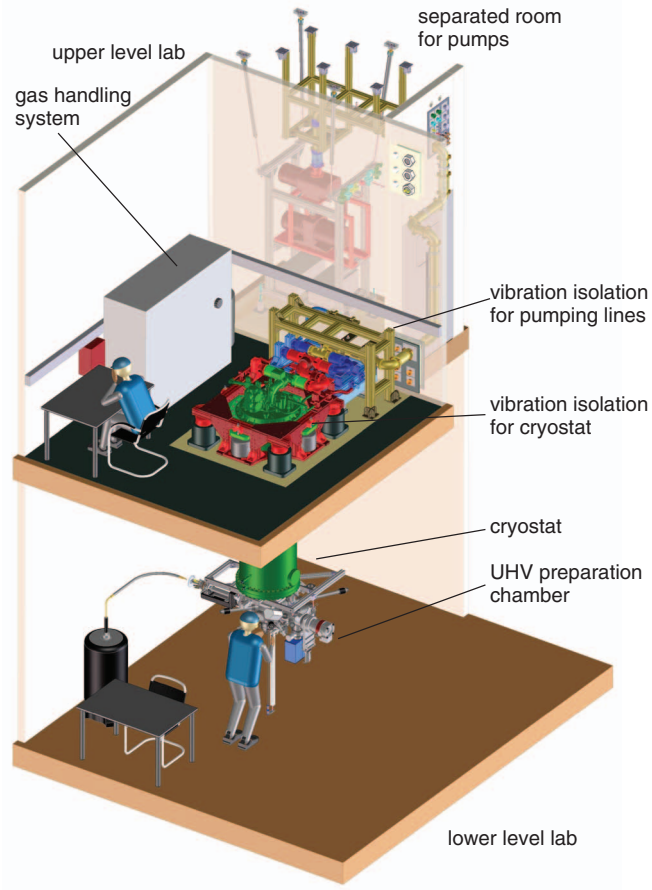

FIG. 13. Overview of the mK-STM setup. The cryostat rests on a vibration isolation stage in the upper level lab. It hangs through the ceiling into the lower level lab with the UHV preparation chamber attached at the bottom. The pumps are located in a separate room hanging from the ceiling to avoid mechanical disturbances on the floor, on which the vibration isolation is placed.

damping stage decouples the cryostat (green). To reduce the vibrational noise of the 1 K-pot-, nitrogen- and dilution cycle-pumps, we used flexible hoses for the connections to the cryostat. All pumping lines and cables are fixed on a heavy granite block (blue), which itself is isolated from the floor with active dampers, before going to the cryostat. For the still pumping line, which has the largest diameter (100 mm), soft bellows were arranged in an opposing configuration in order to compensate the vacuum forces, when crossing over the different damping stages (see Fig. 12).[45] All pumps are placed in a separated acoustically shielded room.

An overview of the complete setup is depicted in Fig. 13. The cryostat including the UHV chamber is supported at the floor of the upper level lab. From this lab, we handle cryostat and STM. The UHV preparation chamber is accessible from the lab below. Tips and samples are transferred from here as well.

V. PERFORMANCE

To verify the stability of our STM, we performed topographic measurements at temperatures of 800 mK and 15 mK (MC temperature). An Au(111) surface measured at 800 mK

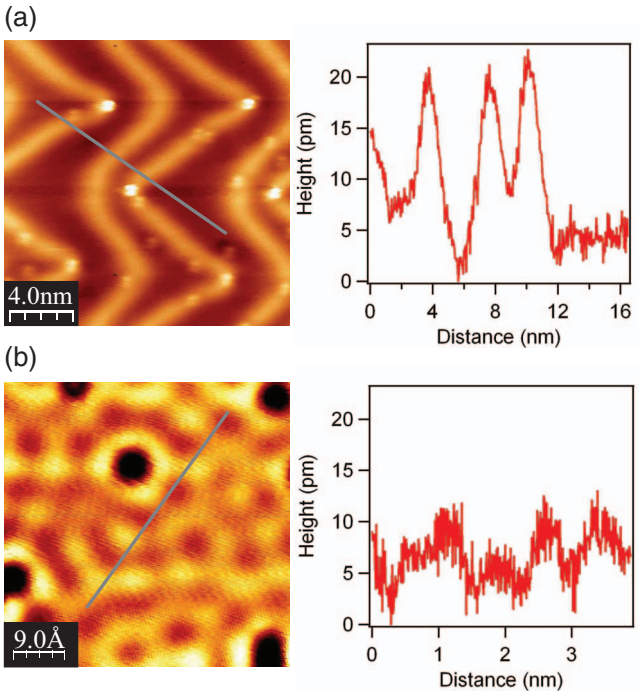

FIG. 14. (a) Topography of Au(111) measured at $T = 800$ mK. (b) Topography of Cu(111) with standing wave pattern of the scattered surface state measured at $T = 15$ mK. $V = 50$ mV, $I = 50$ pA.

is shown in Fig. 14(a). The noise level can be seen in the line profiles across the image, from which we estimated the noise in the z-direction to be about 3 pm. The averaging time per data point during this measurement was 4.2 ms. For lower temperatures, we operate the ^{3}He flow at the lowest circulation rate resulting in a MC temperature of 15 mK. The 1K-pot was running during all measurements. Figure 14(b) shows a Cu(111) surface measured at this temperature. In the image, the standing wave pattern of the Cu(111) surface state scattered from impurities can be seen. Here, we find a z-noise of 4.2 ± 0.5 pm for an averaging time of 3.5 ms per data point.

To verify the temperature of tip and sample, we have temporarily modified the setup and installed two RuO temperature sensors at the corresponding positions (see Fig. 15). We adjusted the MC temperature of the cryostat to 15 ± 0.5 mK having a ^{3}He flow rate of 43 μmol/s. Under these conditions we measured a temperature of 17 ± 5 mK at the tip and

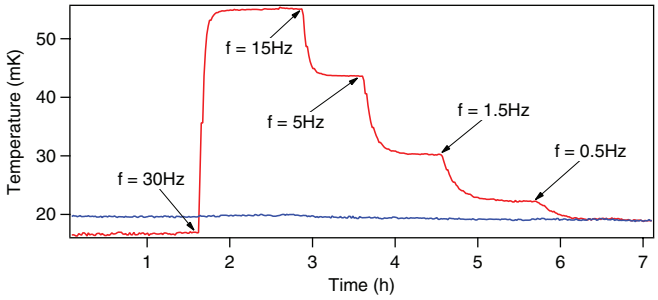

FIG. 15. Temperature measured directly at tip and sample position of the STM. The blue graph shows the sample temperature. The red graph shows the tip temperature. The tip slightly warms up when a sine voltage ($V_{PP} = 5$ V) is applied to the scanning piezo.

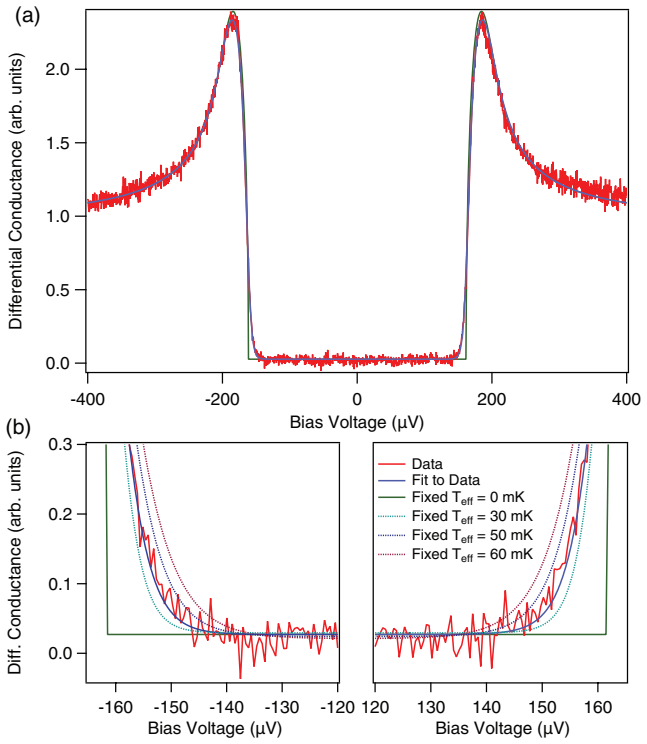

FIG. 16. Measurement of the tunneling conductance between a superconducting Al tip and a Cu(111) surface. (a) The conductance spectrum is shown in red and the fit to the Maki equation is shown in blue. For comparison, a fit at 0 mK is shown in green. (b) Zoom into the corners of the gap. The 0 mK spectrum illustrates that the rounding of the corner is only due to an effective thermal broadening. For comparison, the dotted spectra show a fit to the data for different effective temperatures demonstrating the sensitivity of the fit.

20 ± 5 mK at the sample position using the temperature calibration obtained for the RuO temperature sensors when positioned at the MC. In this context, it should be emphasized again that below about 35 mK the RuO sensor calibration is highly sensitive to the local environment even when the sensor is just moved from the MC to the tip or sample position. The estimated error above accounts for this uncertainty. In this configuration, we checked the temperature evolution during a simulated scan by applying a 5 V_{pp} sine-signal to the z-electrode of the scanning piezo equivalent to a tip displacement of 2 nm perpendicular to the sample surface. Using a frequency of 30 Hz, we observed an increase in the tip temperature to about 55 mK, due to the heat released from the scanning piezo. Decreasing the frequency in steps resulted in a stepwise lowering of the tip temperature. The sample temperature stayed constant during this experiment showing that the heat generated by the piezo does not affect the sample.

To verify the energy resolution of the STM, we measure the superconducting gap of aluminum.[46] Aluminum is ideally suited because it is a weakly coupling superconductor with a nearly isotropic gap.[47–49] Therefore, we expect broadening effects to be mainly due to the finite temperature of the normal conducting Cu(111) sample as well as the experimental broadening.

We prepare our Al tips from high purity Al wire having a diameter of 0.25 mm. The tips are cut under ambient conditions and immediately transferred into vacuum. The oxide layer is removed by Ar ion sputtering without further annealing. If necessary, we have used field emission treatments for further modification of the tip. Tunneling spectroscopy measurements were done on a Cu(111) surface, which was cleaned by cycles of Ar ion sputtering and annealing. A representative measurement at $T_{MC} = 15$ mK is shown in Fig. 16(a). With a superconducting transition temperature of $T_C = 1.2$ K, the conductance spectrum shows a fully developed gap at 15 mK with a value of $\Delta = 183.3\ \mu$eV. All electrons at the Fermi level are condensed in the BCS ground state.

TABLE III. Fitting coefficients of the tunneling conductance between an Al tip and a Cu(111) surface. The DOS was calculated using the Maki equation which is explained in the text. Here Δ is the superconducting gap, ξ is the pair-braking parameter originating from the Maki theory, and T is the effective temperature. The energy resolution $\Delta E = 3.5 k_B T_{\text{eff}}$ has been calculated from the effective temperature.

Δ (μeV)	ζ	T_{eff} (mK)	ΔE (μeV)
183.3 ± 0.1	0.023 ± 0.001	38 ± 1	11.4 ± 0.3

To describe the DOS of the superconducting tip we have used the Maki equation.[50] Spin-orbit scattering effects cancel out as we do not apply any magnetic field (see the Appendix and Ref. 51). The orbital pair breaking parameter ζ reduces the singularities in the coherence peaks to finite values, but maintains a sharp edge in the corners of the gap. The thermal broadening of the measured conductance spectra is accounted for by a convolution of the Maki equation with the derivative of the Fermi-Dirac distribution of the metal substrate. This means that the only rounding of the corner in the gap is due to thermal broadening. Other contributions, such as experimental broadening, noise, or the gap anisotropy, will have a similar effect on the spectrum as the thermal broadening. Therefore, we regard the temperature parameter in this fit function as an effective temperature. It gives an estimate of the upper limit for the energy resolution. The resulting fit function is superimposed onto the conductance spectrum in Fig. 16(a) (blue line). The fitting parameters are summarized in Table III. From the fit we find an effective temperature of $T = 38 \pm 1$ mK corresponding to an energy resolution of $\Delta E = 3.5 k_B T_{\text{eff}} = 11.4 \pm 0.3\ \mu$eV. To better show the quality of the agreement, the corners of the gap are magnified in Fig. 16(b). The rounding of the corners can clearly be attributed to the effective thermal and experimental broadening as the corner becomes sharp at 0 mK (green line). Different fits (dotted lines), where the effective temperature was held fixed at values between 30 mK and 60 mK demonstrate the sensitivity of the fit function to changes in the effective temperature. We would like to point out that no internal cryogenic signal filtering has been implemented.

VI. CONCLUSION

We have presented the design and performance of an STM operating at temperatures of 10 mK. This is realized by attaching the STM unit to a dilution cryostat. Tips and samples can be transferred *in situ* from the UHV chamber into the STM. In this setup, we can apply high magnetic fields of

14 T perpendicular and 0.5 T parallel to the sample surface. We estimated the electronic resolution by analyzing tunneling spectra between a superconducting Al tip and a normal metal sample resulting in an energy resolution of 11.4 μeV. In this way, the lowest possible energy scales, such as the Zeeman splitting or the hyperfine splitting, become observable. This opens up exciting new possibilities for spectroscopy on a local scale.

ACKNOWLEDGMENTS

We gratefully acknowledge the technical support throughout the construction phase by A. Koch and P. Andler as well as fruitful discussions with V. Shvarts and Z. Zhao. C.R.A. acknowledges funding from the Emmy-Noether-Program of the Deutsche Forschungsgemeinschaft (DFG).

APPENDIX: SIMPLIFIED MAKI-EQUATION

We used the Maki formalism to calculate the superconducting quasiparticle DOS.[50,51] Without an external magnetic field the DOS $\rho(E)$ reduces to

$$\rho(E) = \mathrm{Re}\left(\frac{u}{\sqrt{u^2-1}}\right) \tag{A1}$$

with u defined by the following nonlinear equation:

$$u = \frac{E}{\Delta} + \zeta\frac{u}{\sqrt{1-u^2}}. \tag{A2}$$

The quantity ζ is the pair breaking parameter. It is possible to solve Eq. (A2) analytically

$$u = \frac{1}{2}\left(|\epsilon| + \sqrt{1-\zeta^2+d} + \sqrt{1+\epsilon^2-\zeta^2-d-\frac{2|\epsilon|(1+\zeta^2)}{\sqrt{1-\zeta^2+d}}}\right), \tag{A3}$$

where the following abbreviations are used

$$\epsilon = \frac{E}{\Delta},$$
$$b = \epsilon^2 + \zeta^2 - 1,$$
$$c = 108\epsilon^2\zeta^2 + 2b^3 + \sqrt{(108\epsilon^2\zeta^2 + 2b^3)^2 - 4b^6},$$
$$d = \frac{b}{3} + \frac{2^{1/3}b^2}{3c^{1/3}} + \frac{c^{1/3}}{3\cdot 2^{1/3}}.$$

Convolving Eq. (A1) with the Fermi function derivative yields the fit function.

[1] G. Binnig, H. Rohrer, C. Gerber, and E. Weibel, Appl. Phys. Lett. **40**, 178 (1982).
[2] G. Binnig, H. Rohrer, C. Gerber, and E. Weibel, Phys. Rev. Lett. **49**, 57 (1982).
[3] G. Binnig, H. Rohrer, C. Gerber, and E. Weibel, Phys. Rev. Lett. **50**, 120 (1983).
[4] A. Richardella, P. Roushan, S. Mack, B. Zhou, D. A. Huse, D. D. Awschalom, and A. Yazdani, Science **327**, 665 (2010).
[5] K. J. Franke, G. Schulze, and J. I. Pascual, Science **332**, 940 (2011).
[6] S. Loth, S. Baumann, C. P. Lutz, D. M. Eigler, and A. J. Heinrich, Science **335**, 196 (2012).
[7] M. F. Crommie, C. P. Lutz, and D. M. Eigler, Nature (London) **363**, 524 (1993).
[8] C. J. Chen, *Introduction to Scanning Tunneling Microscopy* (Oxford University Press, 1993).
[9] L. Diekhöner, M. A. Schneider, A. N. Baranov, V. S. Stepanyuk, P. Bruno, and K. Kern, Phys. Rev. Lett. **90**, 236801 (2003).
[10] D. Vion, P. F. Orfila, P. Joyez, D. Esteve, and M. H. Devoret, J. Appl. Phys. **77**, 2519 (1995).
[11] F. Delgado and J. Fernandez-Rossier, Phys. Rev. Lett. **107**, 076804 (2011).
[12] R. Meservey, P. M. Tedrow, and P. Fulde, Phys. Rev. Lett. **25**, 1270 (1970).
[13] P. M. Tedrow and R. Meservey, Phys. Rev. Lett. **26**, 192 (1971).
[14] P. Fulde, Adv. Phys. **22**, 667 (1973).
[15] N. Moussy, H. Courtois, and B. Pannetier, Rev. Sci. Instrum. **72**, 128 (2001).
[16] H. Suderow, I. Guillamon, and S. Vieira, Rev. Sci. Instrum. **82**, 033711 (2011).
[17] M. Marz, G. Goll, and H. v. Löhneysen, Rev. Sci. Instrum. **81**, 045102 (2010).
[18] T. Matsui, H. Kambara, and H. Fukujama, J. Low Temp. Phys. **121**, 803 (2000).
[19] Y. J. Song, A. F. Otte, V. Shvarts, Z. Zhao, Y. Kuk, S. R. Blankenship, A. Band, F. M. Hess, and J. A. Stroscio, Rev. Sci. Instrum. **81**, 121101 (2010).
[20] M. Assig, "Development of a Millikelvin scanning tunneling microscope for applications in ultra high vacuum and high magnetic fields (No 5204)," Ph.D. dissertation, École Polytechnique Fédérale de Lausanne, 2011.
[21] C. R. Ast, M. Assig, A. Ast, and K. Kern, Rev. Sci. Instrum. **79**, 093704 (2008).
[22] *attocube systems AG*. ANPz50/LT/UHV z-positioner.
[23] H. London, in *Proceedings of International Conference on Low Temperature Physics* (International Union of Pure and Applied Physics, Oxford, UK, 1951), p. 157.
[24] H. London, G. R. Clarke, and E. Mendoza, Phys. Rev. **128**, 1992 (1962).
[25] T. P. Das, R. de Bruyn Ouboter, and K. W. Taconis, in *Proceedings of 9th International Conference on Low Temperature Physics* (Plenum Press, 1965), p. 1253.
[26] O. V. Lounasmaa, *Experimental Principles and Methods Below 1K* (Academic Press Inc., 1974).
[27] F. Pobell, *Matter and Methods at Low Temperatures*, 3rd ed. (Springer, 2007).
[28] J. C. Wheatley, Am. J. Phys. **36**, 181 (1968).
[29] J. C. Wheatley, O. E. Vilches, and W. R. Abel, Phys. **4**, 1 (1968).
[30] J. C. Wheatley, R. E. Rapp, and R. T. Johnson, J. Low Temp. Phys. **4**, 1 (1971).
[31] V. Shvarts, Z. Zhao, L. Bobb, and M. Jirmanus, J. Phys.: Conf. Ser. **150**, 012046 (2009).
[32] P. R. N. Childs, J. R. Greenwood, and C. A. Long, Rev. Sci. Instrum. **71**, 2959 (2000).
[33] M. Watanabe, M. Morishita, and Y. Ootuka, Cryogenics **41**, 143 (2001).
[34] W. Schoepe, Physica B **165**, 299 (1990).
[35] M. Affronte, M. Campani, S. Piccinini, M. Tamborin, B. Morten, M. Prudenziati, and O. Laborde, J. Low Temp. Phys. **109**, 461 (1997).
[36] G. E. Pike and C. H. Seager, J. Appl. Phys. **48**, 5152 (1977).
[37] I. Batko, K. Flachbart, M. Somora, and D. Vanicky, Cryogenics **35**, 105 (1995).
[38] The inductance is measured with an Agilent 4263B LCR meter. The excitation voltage is 100 mV at a lock-in frequency of 120 Hz.
[39] D. S. Greywall and P. A. Busch, Rev. Sci. Instrum. **60**, 471 (1989).
[40] The resistances are measured with the Lakeshore 370S resistance bridge. The excitation voltages range from 632 μV at the 1 K-pot to 20 μV at the mixing chamber. The lock-in frequency is 9.8 Hz.
[41] S. N. Mott, *Conduction in Non-Crystalline Materials* (Oxford University Press, 1993).
[42] A. L. Efros and B. I. Shklovskii, J. Phys. C **8**, L49 (1975).
[43] *Spectrum control Inc.* 51-726-017.
[44] *Spectrum control Inc.* 1289-004.
[45] W. P. Kirk and M. Twerdochlib, Rev. Sci. Instrum. **49**, 765 (1978).
[46] I. Guillamon, H. Suderow, S. Vieira, and P. Rodiere, Physica C **468**, 537 (2008).
[47] T. Kiss, T. Yokoya, A. Chainani, S. Shin, T. Hanaguri, M. Nohara, and H. Takagi, Nat. Phys. **3**, 720 (2007).
[48] I. Guillamon, H. Suderow, S. Vieira, L. Cario, P. Diener, and P. Rodiere, Phys. Rev. Lett. **101**, 166407 (2008).
[49] Y. Noat, T. Cren, F. Debontridder, D. Roditchev, W. Sacks, P. Toulemonde, and A. S. Miguel, Phys. Rev. B **82**, 014531 (2010).
[50] K. Maki, Prog. Theor. Phys. **32**, 29 (1964).
[51] D. C. Worledge and T. H. Geballe, Phys. Rev. B **62**, 447 (2000).